Molecular mechanism underlying transport and allosteric inhibition of bicarbonate transporter SbtA

Sunzhenhe Fang[a,b,1] ✆, Xiaowei Huang[a,b,1] ✆, Xue Zhang (张雪)[a,1,2] ✆, Minhua Zhang[a], Yahui Hao[a,b], Hui Guo[a], Lu-Ning Liu[c] ✆, Fang Yu[d], and Peng Zhang[a,2] ✆

[a]National Key Laboratory of Plant Molecular Genetics, Center for Excellence in Molecular Plant Sciences, Institute of Plant Physiology and Ecology, Chinese Academy of Sciences, Shanghai 200032, China; [b]University of Chinese Academy of Sciences, 100039 Beijing, China; [c]Institute of Systems, Molecular and Integrative Biology, University of Liverpool, L69 7ZB Liverpool, United Kingdom; and [d]Shanghai Key Laboratory of Plant Molecular Sciences, College of Life Sciences, Shanghai Normal University, Shanghai 200234, China

SbtA is a high-affinity, sodium-dependent bicarbonate transporter found in the cyanobacterial CO_2-concentrating mechanism (CCM). SbtA forms a complex with SbtB, while SbtB allosterically regulates the transport activity of SbtA by binding with adenyl nucleotides. The underlying mechanism of transport and regulation of SbtA is largely unknown. In this study, we report the three-dimensional structures of the cyanobacterial *Synechocystis* sp. PCC 6803 SbtA–SbtB complex in both the presence and absence of HCO_3^- and/or AMP at 2.7 Å and 3.2 Å resolution. An analysis of the inward-facing state of the SbtA structure reveals the HCO_3^-/Na^+ binding site, providing evidence for the functional unit as a trimer. A structural comparison found that SbtA adopts an elevator mechanism for bicarbonate transport. A structure-based analysis revealed that the allosteric inhibition of SbtA by SbtB occurs mainly through the T-loop of SbtB, which binds to both the core domain and the scaffold domain of SbtA and locks it in an inward-facing state. T-loop conformation is stabilized by the AMP molecules binding at the SbtB trimer interfaces and may be adjusted by other adenyl nucleotides. The unique regulatory mechanism of SbtA by SbtB makes it important to study inorganic carbon uptake systems in CCM, which can be used to modify photosynthesis in crops.

bicarbonate transporter | CO_2-concentrating mechanism | allosteric inhibition | structure | photosynthesis

Cyanobacteria have evolved a unique CO_2-concentrating mechanism (CCM) in carbon fixation. This increases the intracellular concentration of CO_2 feeding ribulose bisphosphate carboxylase-oxygenase (RuBisCO) that is encapsulated in carboxysomes, improving photosynthetic performance (1, 2). The CCM contains five distinct uptake systems that transport dissolved inorganic carbon (Ci), HCO_3^-, and CO_2 into the cell (3). Among them, SbtA and BicA are sodium-dependent HCO_3^- transporters with high affinity and medium affinity, respectively (4, 5). BCT1, or CmpABCD, is a HCO_3^- transporter complex powered by ATP hydrolysis (6), while NDH-I$_3$ and NDH-I$_4$ complexes are responsible for CO_2 uptake (7, 8). These Ci uptake systems are ideal targets for enhancing photosynthesis in C3 plants (9–14).

Ci uptake systems are regulated at different levels to adapt to a changing environment. CmpABCD was first identified as a cyanobacterial Ci transporter whose expression level is induced by Ci limitation (6), as are SbtA and NDH-I$_3$, which are regulated by the LysR-type transcription factor NdhR (15). The molecular mechanism underlying transcriptional regulation has previously been studied (16). As a transcription repressor, NdhR controls the expression levels of *ndh-I₃*, *BicA*, and *SbtA/B*, while the Ci limitation metabolite 2-phosphoglycerate can bind to NdhR to alter its conformation and release repression.

Ci transporter activity is allosterically or posttranslationally regulated. SbtA forms a complex with SbtB, while SbtB regulates the transport of SbtA via binding with AMP or cAMP (17). The active form of BicA is a dimer stabilized by the C-terminal sulfate transporter and anti-sigma factor antagonist (STAS) domain; however,

this activity could not be reconstructed in a heterologous expression system (18, 19). This suggests that transporter activity could require additional regulatory proteins or posttranslational modification. In addition, it is considered that the CmpABCD transporter activity is regulated by the cytoplasmic HCO_3^- concentration since the CmpC subunit contains an extra substrate-binding domain in addition to the nucleotide-binding domain (3). The molecular mechanisms of transport and activity regulation of Ci transporters remain largely unknown, which, to a large extent, limits their application in photosynthesis improvement (20–22).

This study focuses on the structural and mechanistic analysis of the bicarbonate transporter SbtA by determining its complex structure with the regulatory subunit SbtB, both in the presence and absence of HCO_3^- and/or AMP. A structure-based analysis suggests molecular mechanisms underlying transport and regulation.

Results

SbtA Activity and Allosteric Inhibition by SbtB. *Can* encodes the carbonic anhydrase, which is required for the growth of *Escherichia coli* under normal air conditions; a *can* paralog, *cynT*, can replace *can* for normal growth when induced with azide (23). This finding was used successfully for active bicarbonate transporter screening (24). We generated the *can* knockout strain using *E. coli* C43(DE3) [C43(DE3)-Δ*can*], which was used to characterize the activity of *Synechocystis* sp. PCC 6803 SbtA, SbtA–SbtB, and its derivative

---

Significance

SbtA is a sodium-dependent, high-affinity bicarbonate transporter in the cyanobacterial CO_2-concentrating mechanism (CCM). The transport activity of SbtA is regulated by SbtB, which is additionally influenced by adenyl nucleotides. We determined the three-dimensional structures of SbtA in complex with SbtB in two different conformations: A model summarizing the molecular mechanism of transport and allosteric inhibition of SbtA was established based on structural and biochemical data. The transport and regulatory mechanism revealed by our study represents a valuable case to investigate allosteric regulation of membrane transporters and, more importantly, will benefit plant photosynthesis improvement using the CCM system.

mutations. Consistent with previous results, the C43(DE3)-Δcan strain cannot grow under normal air conditions but can grow in the presence of 1 mM azide (*SI Appendix*, Fig. S1). The transfer of the SbtA gene into C43(DE3)-Δcan partially complements growth failure under normal air conditions, but the cotransfer of SbtA and SbtB genes fails to do so (Fig. 1 A and B). This suggests that *Synechocystis* sp. PCC 6803 SbtA alone possesses bicarbonate transporter activity when it is expressed in *E. coli* C43(DE3), while SbtB allosterically inhibits transporter activity, which is consistent with previous studies (24).

Overall Structure of SbtA in Complex with SbtB. To obtain SbtA and SbtB protein complex for structural analysis, we coexpressed the *Synechocystis* sp. PCC 6803–originated *SbtA* and *SbtB* in *E. coli* C43 (DE3). We found that the addition of 2 mM AMP or ADP but not cAMP or ATP in the purification buffer was necessary for a stable 1:1 molar ratio complex formation (Fig. 2A). This is consistent with previous results suggesting that the membrane association of SbtB depends on the presence of AMP/ADP but not on cAMP (17). The purified SbtA–SbtB complex protein sample was used for both cryo-electron microscopy (cryo-EM) and crystallization analysis. The cryo-EM structure of SbtA–SbtB complex was obtained in lipid nanodiscs at 2.7 Å resolution (SbtAB^{EM}) (Fig. 2 B and C and *SI Appendix*, Fig. S2 and Table S1). The map quality was high, and numerous additional densities around SbtA were assigned as annular membrane lipids (*SI Appendix*, Fig. S3), allowing us to build an accurate model. The resulting model was then used as a template to determine the crystal structure by molecular replacement, resulting in the 3.2 Å resolution crystal structure of the SbtA–SbtB complex (SbtAB^{Xtal}) (Fig. 2D and *SI Appendix*, Table S2). The overall structures of SbtAB^{EM} and SbtAB^{Xtal} are similar, which form a three-fold complex with a rmsd of 0.635 Å

over 1,178 Cα atoms. SbtA and SbtB form homotrimers in the membrane and cytoplasm, respectively, and each SbtB protomer binds to the cytoplasmic surface of a SbtA protomer to form a heterodimer (Fig. 2 B–D). Similar trimeric transporter structures have been reported in the bacteria ammonium transporter AmtB (25, 26), the glutamate transporter homolog Gltph (27), the human excitatory amino acid transporter EAAT1 (28), and the human concentrative nucleoside transporter CNT3 (29), suggesting that the trimer is the functional unit of SbtA as proposed in other studies (24).

The SbtA molecule in both SbtAB^{EM} and SbtAB^{Xtal} structures is composed of 10 transmembrane helices (TMs). Of these, TMs 1, 4, 6, and 9 are interrupted by short loops (Fig. 2 C and E). The long loop connecting TM5 and TM6 (residues 165 to 207 in SbtAB^{EM} and residues 170 to 207 in SbtAB^{Xtal}), which may be involved in activity regulation (30), is missing in both structures. Both the N and C termini face the periplasm, which confirms the previous experimental results (30). SbtA contains a scaffold domain, consisting of TMs 1 to 2 and 6 to 7, that mediates the interactions between SbtA molecules formed along the trimer. It also contains a core domain consisting of TMs 3 to 5 and 8 to 10 (Fig. 2 C, E, and F). A narrow cleft is present between two domains (Fig. 2F). The SbtB structure is a typical PII fold, characterized by a four antiparallel–stranded β-sheet inserted by two helices, and the long loop comprising residues 40 to 58 (previously named T-loop) is inserted between β2 and β3 (Fig. 2C).

SbtA in both the SbtAB^{EM} and SbtAB^{Xtal} structures is positioned in an inward-facing state. However, the HCO$_3^-$ substrate is clearly defined in each SbtA molecule of the SbtAB^{Xtal} structure but not in the SbtAB^{EM} structure. Three AMP molecules are well defined in the SbtB trimer interfaces of the SbtAB^{EM} structure but are disordered in the SbtAB^{Xtal} structure. Accordingly, the T-loop in the SbtB structure is well defined in the SbtAB^{EM} structure but disordered in the SbtAB^{Xtal} structure (Fig. 2 C and D). Metal ion binding sites, which are supposed to be sodium, are observed in both the SbtAB^{EM} and SbtAB^{Xtal} structures (Fig. 3F and *SI Appendix*, Fig. S4 A and B).

Substrate-Binding Site. Seen from the SbtAB^{Xtal} structure, the substrate HCO$_3^-$ binding site is located at the interface of the core domain and the scaffold domain (Fig. 3A). Two discontinuous TMs, TM4a/4b and TM9a/9b, are surrounded by other TMs and form a TM cross. HCO$_3^-$ binds to the pericentral side of the cross (Fig. 3 A and B and *SI Appendix*, Fig. S4C). The HCO$_3^-$ binding site is accessible from the cytoplasm through a cavity composed of the TMs 2, 6a, 7, and 9b (Fig. 3A). The side chains of residues Ser114 and Ser116 from TM4b and Asp325 and Ser327 from TM9b form hydrogen bonds with HCO$_3^-$ either directly or through a water molecule; the main chain oxygen of Ser324 and two water molecules form hydrogen bonds with HCO$_3^-$ (Fig. 3C). Notably, residues Ser116, Asp325, and Ser327 are subjected to conformational changes in the SbtA molecule of the SbtAB^{EM} structure, which may distort the binding of HCO$_3^-$ (Fig. 3D and *SI Appendix*, Fig. S4 C and D). The mutation of the HCO$_3^-$ binding residue could significantly impair the complementary function of SbtA (Fig. 3E and *SI Appendix*, Fig. S5). On the peripheral side of the TM cross, there was a clear electron density peak that was supposed to be an Na$^+$ binding site (Fig. 3B and *SI Appendix*, Fig. S4 A and B); it forms five bonds [usually seen in sodium-dependent transporters (19, 31)] with the main chain oxygens of residues Phe110, Gly111, and Ala112 from TM4a and Ala-320 and Ser322 from TM9a (Fig. 3F). Most of the residues involved in HCO$_3^-$ and Na$^+$ binding are conserved among cyanobacterial SbtA proteins (*SI Appendix*, Fig. S6), suggesting a conserved binding mode. In summary, the SbtA structures captured in SbtAB^{EM} and SbtAB^{Xtal} complexes represent substrate-free and substrate-binding conformations of the inward-facing state, respectively.
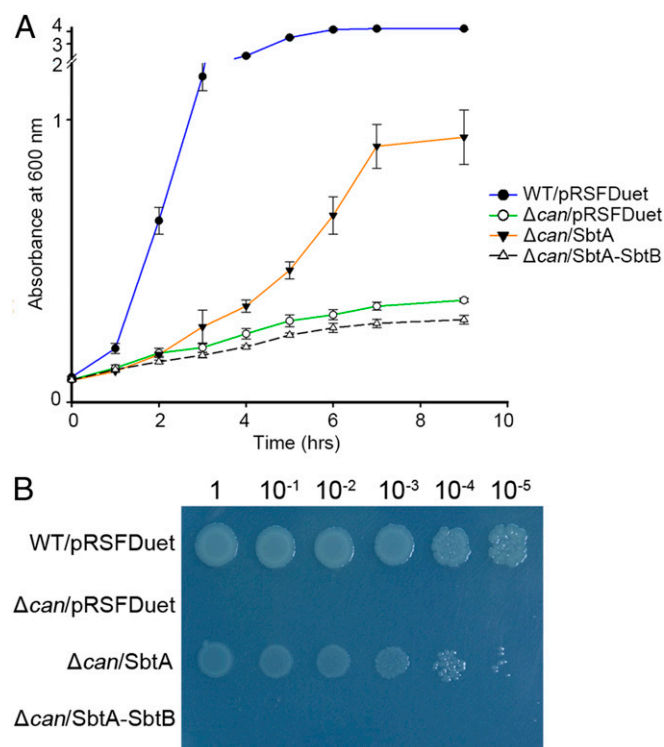

Fig. 1. Functional characterization of SbtA and SbtB. Complementation of the Δcan strain was conducted by expression of *SbtA*, *SbtA-SbtB*, or empty vector as a control. The wild-type strain was used as a positive control. Growth curve (*A*) and dilution spotting assay (*B*) are shown, respectively. The error bars in *A* represent SD, and *n* = 4 technical replicates.

2 of 8 | PNAS
https://doi.org/10.1073/pnas.2101632118

Fang et al.
Molecular mechanism underlying transport and allosteric inhibition of bicarbonate transporter SbtA
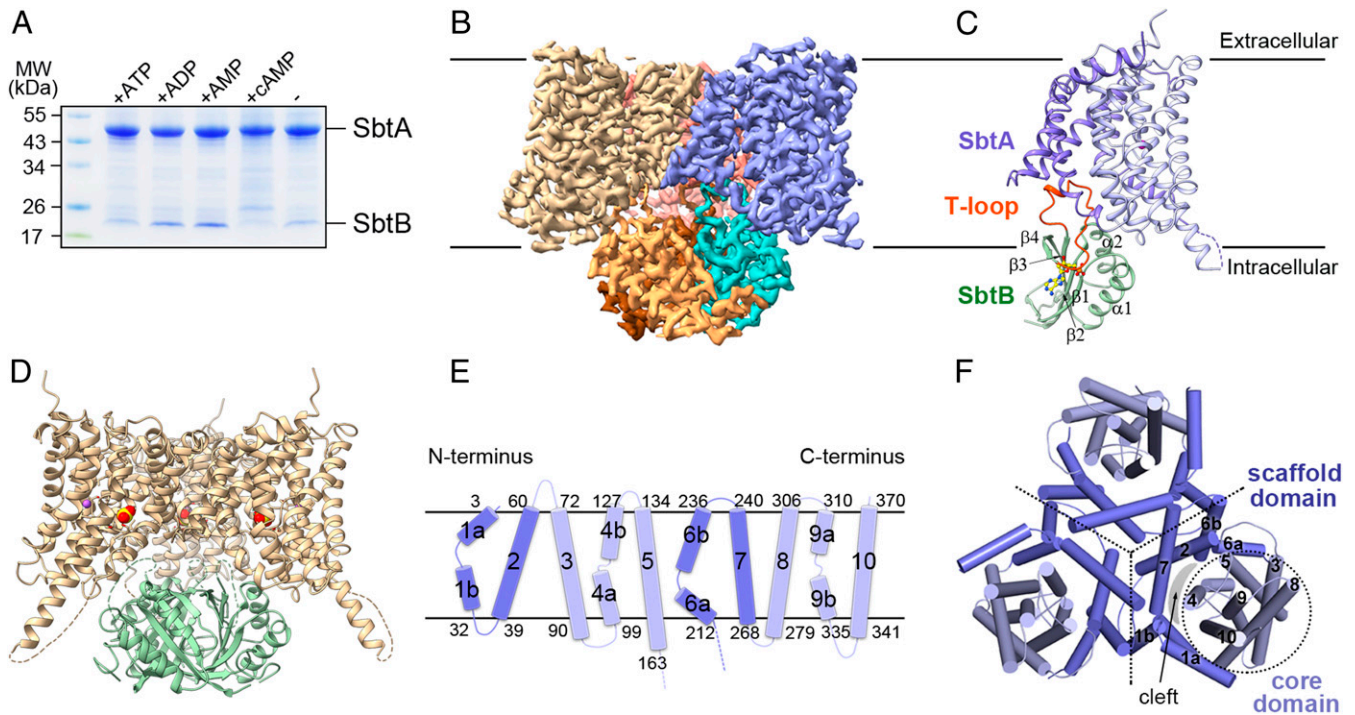
Fig. 2. Overall structure of SbtA–SbtB complex. (*A*) Pull-down assay results show the interaction between SbtA and SbtB with/without the addition of different adenyl nucleotides. A total of 2 mM ATP, 2 mM ADP, 2 mM AMP, or 2 mM cAMP was added to the purification buffer in the assay, respectively. (*B*) Cryo-EM map of SbtAB^{EM} in side view colored by molecules. (*C*) Structure of SbtA–SbtB heterodimer formed in SbtAB^{EM} complex. Structure elements of SbtB are labeled. Scaffold domain of SbtA, slate blue; core domain of SbtA, light blue; SbtB, green; T-loop of SbtB, orange red. (*D*) Crystal structure of SbtAB^{Xtal} presented as a trimer. SbtA, gold; SbtB, green. (*E*) Topology of SbtA. The TMs are numbered from 1 to 10. Numbers indicate the beginning/ending residue positions. (*F*) Extracellular view of SbtA trimer. The scaffold domain and core domain are displayed as cylinders and colored accordingly; the narrow cleft between two domains is indicated by gray shadow.

Interactions between SbtA and SbtB and Functional Role of AMP.
While SbtA and SbtB form similar heterodimers in the SbtAB^{EM} and SbtAB^{Xtal} structures, the interaction surfaces are significantly different. In the SbtAB^{EM} structure, the interaction surface of SbtA and SbtB is clearly defined and buries about 807.4 Å^2 (Fig. 4*A*); it is constituted by the β1-α1 loop, the α2-β4 loop, and the T-loop from SbtB as well as TM2, 7, 9b, and 10 from SbtA. The T-loop of SbtB inserts itself into the cytoplasmic cavity of SbtA constituted by TMs 2, 6a, 7, and 9b, and the interactions are primarily van der Waals' contacts (Fig. 4*A*). Additionally, hydrogen-bonding interactions are found between the side chains of residues Glu265, Ser268, Arg269, and Arg333 from SbtA and the side chains of residues Glu13, Asn52, and Tyr87, the backbones of residues Arg46, Thr53, and Asp86 from SbtB (Fig. 4 *B* and *C*). However, in the SbtAB^{Xtal} structure, the T-loop of SbtB is disordered and the interactions between SbtB and SbtA are restricted to the β1-α1/α2-β4 loops and TM9b, while the interaction surface area is reduced to 127.6 Å^2 (*SI Appendix*, Fig. S7*A*).

We analyzed the determinants stabilizing the SbtB T-loop conformation in the SbtAB^{EM} structure and found that the AMP molecule bound in SbtB plays a critical role (Fig. 4*A*). The AMP binds at the intermolecular cleft of two neighboring SbtB molecules (Fig. 4*D* and *SI Appendix*, Fig. S8), which is similar to the previous SbtB trimeric structure (17, 32). However, a detailed analysis revealed more extensive hydrogen bonds surrounding AMP in our structure (Fig. 4*D*). In particular, the residues Ser42 and Arg43 from the T-loop and the residue Gly89 from the b4 form four hydrogen bonds with the phosphate group of AMP. Additionally, the guanidine group of Arg43 forms a hydrogen bond with the main chain oxygen of residue Asp86 from the α2-β4 loop; Arg46 forms hydrogen bonds with the Arg43 main chain oxygen and Asn59.

These interactions dictate and stabilize the T-loop conformation of SbtB when binding with SbtA.

We identified key residues involved in SbtA–SbtB interactions and AMP binding to perform mutation-based functional analyses. Pull-down results show that the mutant SbtA(R333A)-SbtB almost abolishes the SbtA–SbtB complex formation, while SbtA-SbtB(E13D) impairs complex formation (Fig. 4*E*). Point mutations aiming to reduce the SbtB T-loop interactions with SbtA, such as SbtA(R269A)-SbtB, SbtA(E265A)-SbtB, and SbtA-SbtB(V45L), have relatively minor effects on complex formation, which may be due to their extensive interaction surface areas. However, SbtA-SbtB(S47Q) mutation aiming to introduce steric conflict at the interaction surface disrupts the complex formation (*SI Appendix*, Fig. S7*B*). Furthermore, mutations of residues involving AMP binding, SbtA-SbtB(S42A/R43A) and SbtA-SbtB(R46A), significantly reduce the complex formation (Fig. 4*E*). Accordingly, mutations that abolish the complex formation, such as SbtA-SbtB(S47Q) and SbtA(R333A)-SbtB, could significantly reduce the growth failure of C43(DE3)-Δcan-SbtAB, while mutations that impair the complex formation, such as SbtA-SbtB(E13D), SbtA-SbtB(S42A/R43A), SbtA-SbtB(R46A), and SbtA(E269A)-SbtB, have a positive effect on the growth (Fig. 4*F* and *SI Appendix*, Fig. S9). Therefore, we conclude that the inhibition of SbtA activity by SbtB relies on the SbtA–SbtB complex formation, which is greatly strengthened by AMP binding, as is also proposed in other work (17, 24).

These results provide a molecular explanation for why the addition of AMP during the protein purification greatly enhances the complex formation of SbtA–SbtB (Fig. 2*A*), and they also explain well why the association of SbtB with the membrane largely depends on the presence of AMP (17). To investigate why the addition of cAMP impairs the SbtA–SbtB complex formation,
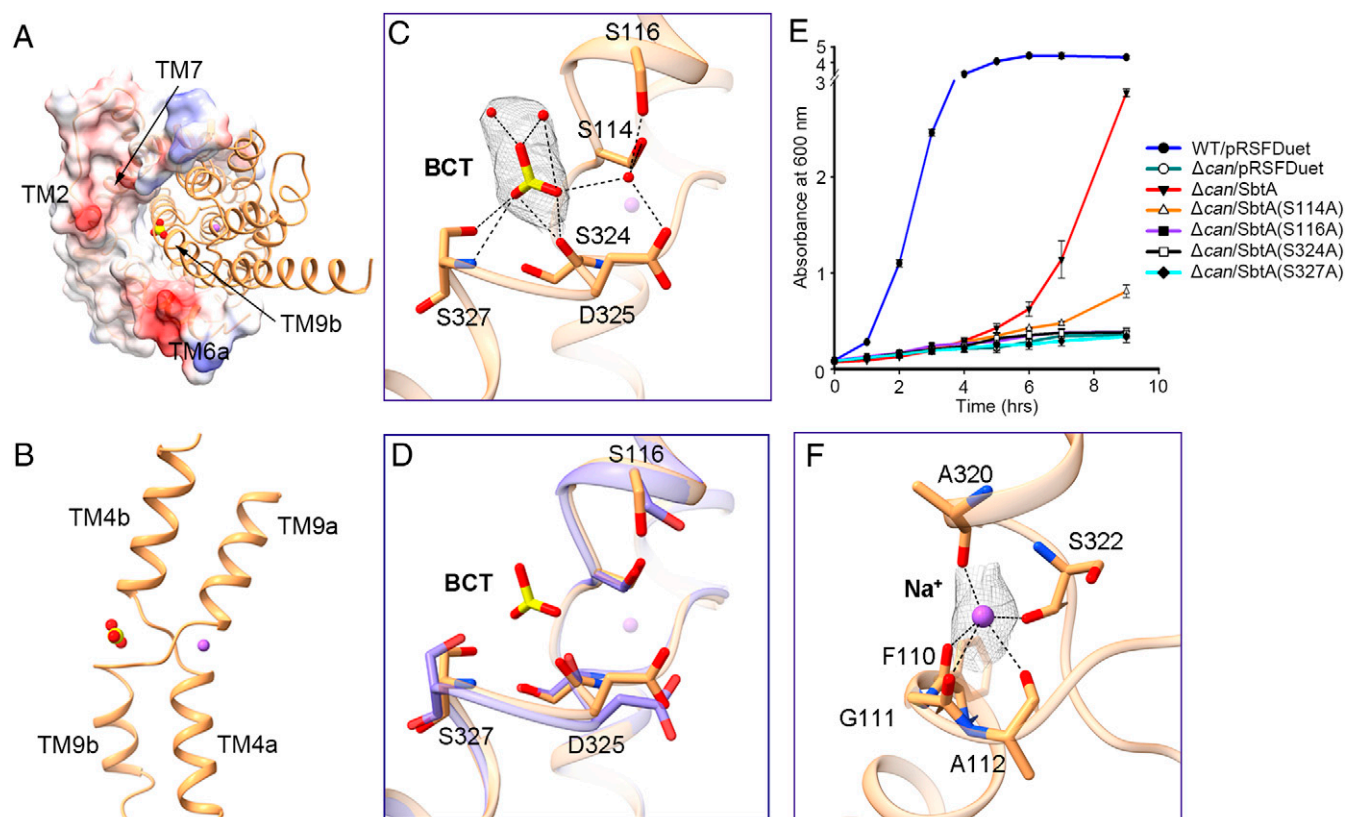
Fang et al.
Molecular mechanism underlying transport and allosteric inhibition of bicarbonate transporter SbtA

PNAS | 3 of 8
https://doi.org/10.1073/pnas.2101632118

Fig. 3. Substrate-binding site of SbtA. (*A*) Intracellular view of the substrate-binding site in the SbtAB^{Xtal} structure. The scaffold domain and core domain are shown in electrostatic surface and ribbon, respectively. Blue and red colors represent positive and negative charges. Bicarbonate and sodium ion are indicated as yellow and purple spheres, respectively. (*B*) TM cross constituted by TM4a/b and TM9a/b. (*C*) Bicarbonate binding site in the SbtAB^{Xtal} structure. Bicarbonate and residues involved in coordination are labeled and shown as sticks. Water molecules are indicated as red spheres. 2Fo-Fc electron densities of bicarbonate and water molecules are contoured at 1.5 σ. (*D*) Comparison of the bicarbonate binding site in SbtAB^{Xtal} (gold) and SbtAB^{EM} (slate blue). (*E*) Growth assay of substrate-binding site mutants in the Δ*can* strain. Complementation of the Δ*can* strain was conducted by the expression of four mutants involved in bicarbonate binding or empty vector as a control. The wild-type strain was used as a positive control. The error bars represent SD, and $n = 3$ technical replicates. (*F*) Sodium binding site in the SbtAB^{Xtal} structure. Residues involved in coordination are labeled and shown as sticks. 2Fo-Fc electron densities of sodium ion are contoured at 1.5 σ.

we superimposed the cAMP molecule to the AMP binding site of the SbtAB^{EM} structure (Fig. 4*G*). Our results suggest that the binding mode of the adenine moiety of cAMP overlaps with AMP, while the hydrogen bonds formed via residues Ser42 and Arg43 may be lost in the presence of cAMP. Additionally, cAMP displays a steric clash with the sidechain of Arg46. These processes could distort the T-loop conformation and diminish SbtA–SbtB interactions.

Transport and Regulatory Mechanism. The TM cross is a typical structural feature of the substrate-binding site in the SbtA protein (Fig. 3*B*) and resembles the structure of some solute carrier (SLC) family transporters. A protein structure comparison via DALI server (33) produced four matches (*z*-score over 10), all of which were sodium-dependent SLC family transporters [NhaA, NhaP, NapA, and ASBT; respective corresponding Protein Data Bank (PDB) accession codes 4atv, 4cz8, 4bwz, and 3zux (34–37)]. These not only share a similar structure feature at the substrate-binding site but also similar overall topology (Fig. 5*A*). Of particular interest is the ASBT$_{NM}$, which is a bacterial homolog (*Neisseria meningitidis*) of the animal sodium-dependent bile acid symporter ASBT (34). While SbtA and ASBT$_{NM}$ only share ~10% sequence identity, both structures contain 10 TMs, and over 80% of their structural elements were aligned. All structures of these transporters contain two domains: a core domain for substrate binding and a scaffold domain for oligomerization. The transport mechanism of these transporters has been proposed based on

their structures (34–38), which could take the form of a rocking bundle or elevator mechanism involving rigid body movement of the core domain between inward-facing and outward-facing states. SbtA could follow a similar transport mechanism (Fig. 5*B*), and the core domain may undergo rigid movement to translocate HCO$_3^-$ into the plasma membrane.

Current and previous results both demonstrate that SbtB can inhibit the bicarbonate transporter activity of SbtA when heterologously expressed in *E. coli* (24) (Fig. 1 *A* and *B*), suggesting that SbtB allosterically inhibits the transport activity of SbtA by forming complexes under certain physiological conditions. An analysis of our structural data reveals the underlying molecular mechanism of the allosteric inhibition of SbtA by SbtB. In the SbtAB^{EM} structure, the SbtA–SbtB interaction surface involves both the core domain and the scaffold domain of SbtA; in particular, the T-loop of SbtB inserts itself into the cytoplasmic cavity formed between the two domains of SbtA. This could preclude the core domain movement during transport and lock SbtA at the inward-facing substrate-free conformation (Fig. 5*B*). However, in the SbtAB^{Xtal} structure, the intermolecular interactions are restricted to the core domain of SbtA due to the disordered T-loop or the absence of AMP in the SbtB molecule (Fig. 5*B*), and the SbtA protein is located in the inward-facing substrate-binding conformation. This implies that the SbtAB^{Xtal} structure could represent a prestep of allosteric inhibition. Therefore, we conclude that high AMP concentrations stabilize the SbtB T-loop
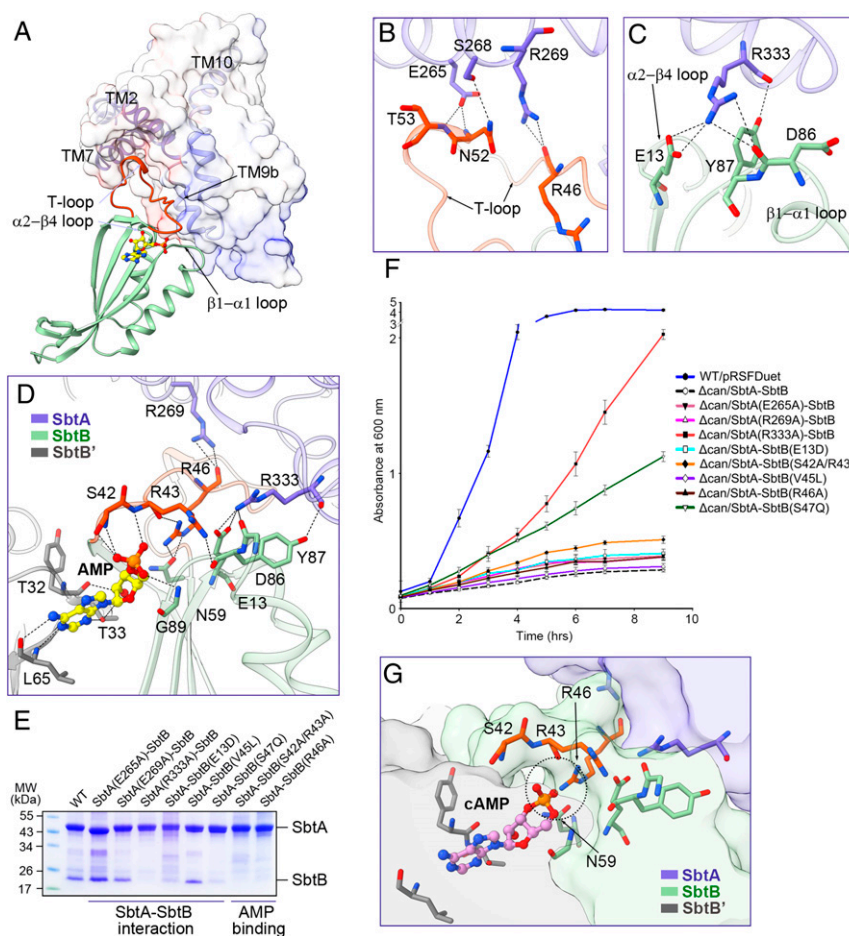
Fig. 4. Interaction between SbtA and SbtB. (A) Side view of SbtA–SbtB interface in SbtAB^{EM} structure. SbtA and SbtB are shown in electrostatic surface and ribbon, respectively. Structure elements involved in SbA–SbtB interaction are labeled. (B and C) Hydrophilic interactions between SbtA and T-loop (B) or b1-a1/a2-b4 loop (C) of SbtB. Residues involved are labeled and shown as sticks. The hydrogen bonds are indicated by dashed lines. (D) A detailed view of AMP binding pocket. The neighboring SbtB molecule is shown and colored in gray. (E) Pull-down assay of SbtAB mutants involved in SbtA–SbtB interaction and AMP binding. (F) Growth assay of SbtAB mutants in the Δcan strain. Complementation of the Δcan strain was conducted by the expression of six SbtAB mutants involved in SbtA–SbtB interaction and two in AMP binding. The wild-type strain was used as a positive control. The error bars represent SD, and $n = 4$ technical replicates. (G) Binding pocket of adenyl nucleotide superimposed with cAMP (pink). The dashed circle shows the conflict between cAMP and SbtB with key residues indicated.

conformation and help insert it into the cytoplasmic cavity of SbtA, which locks the conformation of the scaffold domain and core domain of SbtA in the inward-facing state and inhibits bicarbonate transporter activity. Additionally, the presence of cAMP can compete with AMP to bind with SbtB, inducing conformational change in the T-loop and precluding its interaction with SbtA, relieving SbtB inhibition toward SbtA. Therefore, the T-loop of SbtB could regulate the transporter engine SbtA in response to environmental AMP or cAMP concentration.

Discussion

The mechanism of allosteric regulation of SbtA by SbtB is similar to the regulation of the ammonium transporter AmtB by GlnK in bacteria, where GlnK also forms a trimer with ADP molecules binding at the neighboring dimeric interface to allosterically inhibit the transporter activity of AmtB (39). Both SbtB and GlnK belong to the PII family of proteins, which help regulate various aspects of nitrogen assimilation and carbon homeostasis via binding with adenyl nucleotides (21). This regulation mechanism is found in many different species despite long-term evolution.

Cyanobacterial CCM contains three bicarbonate transporters. Of these, SbtA can be allosterically inhibited by SbtB. The inhibitory

effect relies on the StbA and SbtB complex formation and is adjusted by the adenyl nucleotides binding with SbtB. The presence of AMP stabilizes the SbtA–SbtB complex, while cAMP disrupts the complex (Fig. 2A), as is also shown in other studies (17). The T-loop of SbtB could be involved in the interaction between SbtA and SbtB but is disorganized in structures where SbtB is associated with AMP, ADP, or cAMP (17, 32). Therefore, the structure of how SbtA–SbtB complexes bind with AMP explains the inhibitory mechanism of SbtA by SbtB. A recently reported Ca^{2+}-ATP:SbtB structure from *Cyanobium* sp. 7001 revealed that Ca^{2+} could stabilize the T-loop conformation, which is required for allosteric regulation of SbtA (32). However, additional structural analysis demonstrates that the T-loop conformation in Ca^{2+}-ATP:SbtB structure is different from the structure we outlined and conflicts with SbtA when aligned to the SbtAB^{EM} structure (*SI Appendix*, Fig. S10). These results are consistent with our biochemical data, which demonstrates that the presence of ATP decreases the SbtA–SbtB complex formation (Fig. 2A). The SbtA–SbtB complex was also destabilized by cAMP both in vivo and in vitro, and cAMP was considered a physiologically high carbon signal (21). This seems to be in conflict with the notion that Ci transporter activity can be activated at low carbon levels and inhibited at high
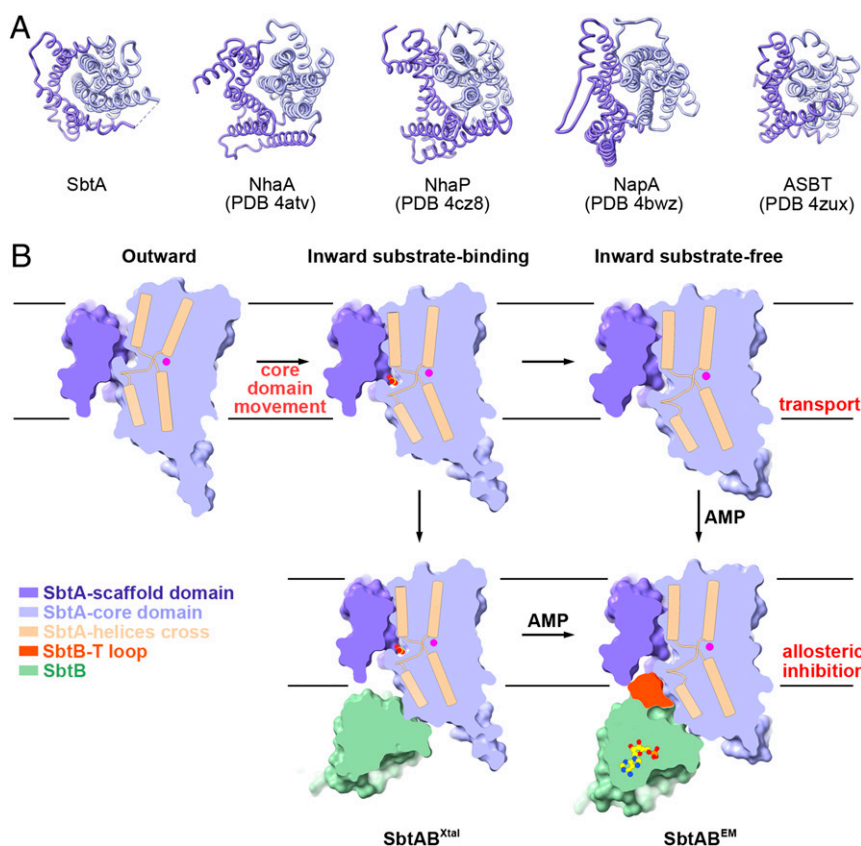
Fang et al.
Molecular mechanism underlying transport and allosteric inhibition of bicarbonate
transporter SbtA

PNAS | 5 of 8
https://doi.org/10.1073/pnas.2101632118

Fig. 5. Transport and regulatory mechanism of SbtA. (*A*) Structure comparison of SbtA with topological homologs. Protomers of SbtA, NhaA, NhaP, NapA, and ASBT are displayed in intracellular view. The scaffold domain and core domain are colored by slate blue and light blue, respectively. (*B*) Proposed transport and regulatory mechanism of SbtA. Distinct conformations are indicated. The top illustrates key conformational states of SbtA during the transport of substrate. In the outward state, the TM cross is exposed to the periplasm, and Na^+-binding may facilitate the binding of substrate. Converting to the inward state, the core domain undergoes rigid movement in order to translocate HCO_3^- into the plasma membrane. The bottom illustrates the allosteric inhibition of SbtA by SbtB. In the presence of AMP, T-loop of SbtB inserts into the cytoplasmic cavity formed between the two domains of SbtA, which locks SbtA at an inward substrate-free state and inhibits the bicarbonate transporter activity.

carbon levels; however, it could accommodate specific physiological environmental transitions (24, 32). The unique regulatory mechanism of SbtA by SbtB makes it important to investigate Ci uptake systems, which could facilitate the photosynthetic modification of CCM in crops (40).

Materials and Methods

Gene Cloning and Protein Purification. The genes encoding SbtA and SbtB were amplified by PCR from *Synechocystis* sp. PCC 6803 genomic DNA. The fragment *SbtA* and *SbtB* were digested with NcoI/SalI and NdeI/XhoI, respectively, and were subsequently ligated into the MCS1 and MCS2 of pRSFDuet plasmid, respectively. The recombinant plasmid pRSFDuet-*SbtA-SbtB*, including a C-terminal His-tag on *SbtA*, was used to transform *E. coli* C43(DE3) for expression. Bacterial cells were grown at 37 °C in Luria broth (LB) medium with 50 μg/mL kanamycin, and protein expression was induced by 0.25 mM β-d-thiogalactopyranoside (IPTG) at around optical density $(OD)_{600} = 1.2$.

After 14 h at 37 °C, the cells were collected and homogenized in buffer A (100 mM NaCl, 20 mM Tris HCl, pH 8.0, 5% [vol/vol] glycerol, and 2 mM AMP) and lysed using a French press. Cell debris was removed by centrifugation. The supernatant was collected and centrifuged using ultracentrifugation at $150,000 \times g$ for 1 h. The membrane fraction was incubated with 1% (wt/vol) n-dodecyl-β-d-maltopyranoside (DDM; Bluepus) for 2 h at 4 °C. After another centrifugation step at $20,000 \times g$ for 45 min, the supernatant was loaded onto an Ni^{2+}-NTA affinity column (Qiagen) and then washed with buffer B (100 mM NaCl, 20 mM Tris-HCl, pH 8.0, 0.018% DDM, and 2 mM AMP) supplemented with 25 mM imidazole. The protein was eluted from the column using buffer B supplemented with 250 mM imidazole and was then concentrated to around 10 mg/mL before further purification by gel

filtration (Superdex-200) in buffer C (100 mM NaCl, 20 mM Tris-HCl, pH 8.0, 0.18% n-decyl-β-d-maltoside [DM; Anatrace], and 2 mM AMP). The peak fraction was collected and concentrated to ~5 mg/mL for crystallization.

Construction of *can* Deletion Mutant. The *can* deletion in the chromosome of *E. coli* was constructed. The upstream and downstream fragments of *can* operon were amplified and overlapped together by PCR, resulting in the replacement fragment Overlap-*can*. The sgRNA plasmid targeting gene *can* pCB003_N20_*can* was obtained from pCB003 by PCR. The plasmid pCB006 was transformed into *E. coli* C43(DE3). Arabinose was added to the culture when preparing the *E. coli*/pCB006 competent cell for recombination. A total of 4 μL Overlap-*can* and 4 μL pCB003_N20_*can* were electroporated into the *E. coli*/pCB006 competent cells. Cells were recovered at 30 °C for 2 h and then spread onto LB agar plates containing kanamycin and spectinomycin and incubated at 30 °C for 24 h. The right colonies were confirmed by DNA sequencing. pCB003 was cured by adding IPTG, and pCB006 was cured by growing at 37 °C overnight.

Growth Assay. C43(DE3) and C43(DE3)-Δ*can* strains were first grown on LB medium supplemented with 50 μg/mL kanamycin and 0.1 mM sodium azide at 37 °C overnight. Seed cells were prepared in LB medium to OD_{600} of 0.1. A total of 1 mL seed cells was added to 20 mL LB medium containing 0.2 mM IPTG and 50 μg/mL kanamycin. Growth was measured at different time slots. For dilution spotting assay, seed cells were diluted by 10^1-, 10^2-, 10^3-, 10^4-, and 10^5-fold, respectively. A total of 2 μL aliquot of each dilution was spotted onto the LB agar plate containing 0.2 mM IPTG and 50 μg/mL kanamycin. Plates were incubated at 37 °C overnight. All tests were repeated at least three times independently.

In Vitro Pull-Down Assays. To analyze the SbtA–SbtB complex formation with the addition of adenyl nucleotides, 2 mM ATP, 2 mM ADP, 2 mM AMP, or 2 mM cAMP was added to the purification buffer. Wild-type SbtA–SbtB or mutations were coexpressed in *E. coli* C43(DE3). After cell disruption and centrifugation, the supernatants were loaded to Ni^{2+}-NTA affinity resin. The nonspecific bound protein was washed off. Target protein was eluted from the resin and examined with sodium dodecyl sulfate polyAcrylamide gel electrophoresis and visualized with Coomassie Blue staining.

Nanodisc Reconstitution. 1-palmitoyl-2-oleoyl-sn-glycero-3-phosphoglycerol (POPG; Avanti) was solubilized in chloroform, dried under argon gas to form a thin lipid film, and stored under vacuum overnight. The lipid film was hydrated and resuspended at a concentration of 10 mM in a buffer containing 20 mM Tris, pH 8.0, 100 mM NaCl, and 100 mM sodium cholate. SbtA–SbtB complex proteins, MSP2N2 membrane scaffold protein, and POPG were mixed at a molar ratio of 1:3:150 in a buffer containing 20 mM Tris, pH 8.0, 100 mM NaCl, 15 mM sodium cholate, and 2 mM AMP and incubated at 4 °C for 1 h. Extra DDM detergent was removed by incubation with 0.6 mg/mL Bio-Beads SM2 (Bio-Rad) at 4 °C overnight. Nanodisc-embedded SbtA–SbtB was purified using a Superdex 200 column in a buffer containing 20 mM Tris, pH 8.0, 100 mM NaCl, and 2 mM AMP.

Cryo-EM Sample Preparation and Data Acquisition. To prepare samples for cryo-EM analysis, 3 μL purified nanodisc-embedded SbtA–SbtB complex at a concentration of 1 mg/mL was applied to glow discharged carbon grids (Quantifoil Cu R1.2/1.3). Grids were blotted for 3 s and plunge-frozen in liquid ethane cooled by liquid nitrogen using a Vitrobot Mark IV (Thermo Fisher) at 8 °C and 100% humidity. The prepared grids were transferred to a Titan Krios electron microscopy operating at 300 kV equipped with Gatan K3 detector and GIF Quantum energy filter. The movie stacks were recorded in the superresolution mode at nominal magnification of 81,000× with a calibrated pixel size of 0.539 Å. The defocus range was from −1.8 to −1.5 μm. Each stack of 32 frames was exposed for 2.56 s with a total dose rate of ~50 $e^-/Å^2$. AutoEMation was used for automated data collection (41). All 32 frames in each stack were aligned using MotionCor2 (42) and binned to a pixel size of 1.0773 Å. The defocus value of each image was determined by Gctf (43).

Data Processing. A total of 3,186,493 particles were automatically picked using RELION 3.0 (44) from 2,971 micrographs. After two rounds of two-dimensional classification, ~20% of the selected particles were used to generate an initial model by RELION 3.0. With particles rescaled to 128 pixels, one good reference and three bad references were generated after three-dimensional (3D) classifications. The good class from the last four iterations yielded a dataset containing 268,921 particles, giving rise to reconstruction at 3.4 Å resolution with C3 symmetry applied. The dataset was then subjected to local search multireference 3D classification, and the multireference models were generated using the reconstruction low-pass filtered to 5 to 30 Å. Particles from good classes were merged and duplicated particles were removed, and another round of multireference classification using bin1 particles yielded a dataset containing 125,998 particles, resulting in reconstruction at 3.1 Å. The application of a solvent mask for further postprocessing improved resolution to 2.7 Å.

The overall resolutions were estimated based on the gold-standard Fourier shell correlation = 0.143 criterion. The details related to data processing are summarized in *SI Appendix*, Fig. S2 and Table S1.

Model Building and Structure Refinement. The atomic coordinate of SbtAB complex was generated by combining homology modeling and de novo model building. The initial structure model of SbtA was predicted by protein structure prediction server trRosetta (45), and the crystal structure of SbtB (17) (PDB code 5O3S) was used. The structure of SbtAB complex was docked into the density map and manually adjusted and rebuilt by COOT (46). The resulting model was refined by phenix.real_space_refine program in PHENIX (47) with secondary structure and geometry restraints. The structure was validated with MolProbity (48), and refinement statistics are shown in *SI Appendix*, Table S1. All structure figures were prepared in ChimeraX (49).

Crystallization, Data Collection, and Determination of Structure. SbtA–SbtB complex was concentrated to 5 mg/mL and crystallized via vapor diffusion at 20 °C in 96-well sitting-drop plates. The best crystals were grown in 0.05 M magnesium chloride, 0.1 M glycine pH 9.0, and 22% polyethylene glycol 400 (the protein:reservoir volume in a ratio of 1:1) and were directly flash-frozen in liquid nitrogen for data collection. All data were collected at BL19U1 beamline of the Shanghai Synchrotron Radiation Facility under 100 K liquid nitrogen stream (wavelength = 0.9798 Å) and processed using HKL-3000 (50). The SbtA–SbtB complex crystallized in space group H32 with cell parameters a = 107.2 Å, b = 107.2 Å, and c = 352.2 Å.

The complex structure was solved by molecular replacement with PHENIX, using the SbtAB^{EM} structure (PDB code 7EGK) as an initial model. The model was manually built in COOT, refined with PHENIX, and validated using MolProbity. A summary of data collection and refinement statistics is provided in *SI Appendix*, Table S2.

Data Availability. The atomic coordinates of SbtAB^{Xtal} have been deposited in PDB with accession code 7EGL. The cryo-EM map and atomic coordinates of SbtAB^{EM} have been deposited in the Electron Microscopy Data Bank (EMD-31135) and PDB (7EGK). All other study data are included in the article and/or *SI Appendix*.

1. M. Giordano, J. Beardall, J. A. Raven, CO_2 concentrating mechanisms in algae: Mechanisms, environmental modulation, and evolution. *Annu. Rev. Plant Biol.* **56**, 99–131 (2005).
2. G. D. Price, M. R. Badger, F. J. Woodger, B. M. Long, Advances in understanding the cyanobacterial CO_2-concentrating-mechanism (CCM): Functional components, Ci transporters, diversity, genetic regulation and prospects for engineering into plants. *J. Exp. Bot.* **59**, 1441–1461 (2008).
3. G. D. Price, Inorganic carbon transporters of the cyanobacterial CO_2 concentrating mechanism. *Photosynth. Res.* **109**, 47–57 (2011).
4. M. Shibata et al., Genes essential to sodium-dependent bicarbonate transport in cyanobacteria: Function and phylogenetic analysis. *J. Biol. Chem.* **277**, 18658–18664 (2002).
5. G. D. Price, F. J. Woodger, M. R. Badger, S. M. Howitt, L. Tucker, Identification of a SulP-type bicarbonate transporter in marine cyanobacteria. *Proc. Natl. Acad. Sci. U.S.A.* **101**, 18228–18233 (2004).
6. T. Omata et al., Identification of an ATP-binding cassette transporter involved in bicarbonate uptake in the cyanobacterium *Synechococcus* sp. strain PCC 7942. *Proc. Natl. Acad. Sci. U.S.A.* **96**, 13571–13576 (1999).
7. M. Shibata et al., Distinct constitutive and low-CO2-induced CO2 uptake systems in cyanobacteria: Genes involved and their phylogenetic relationship with homologous genes in other organisms. *Proc. Natl. Acad. Sci. U.S.A.* **98**, 11789–11794 (2001).
8. S. Maeda, M. R. Badger, G. D. Price, Novel gene products associated with NdhD3/D4-containing NDH-1 complexes are involved in photosynthetic CO2 hydration in the cyanobacterium, Synechococcus sp. PCC7942. *Mol. Microbiol.* **43**, 425–435 (2002).
9. N. Mangan, M. Brenner, Systems analysis of the CO_2 concentrating mechanism in cyanobacteria. *eLife* **3**, e02043 (2014).
10. S. P. Long, A. Marshall-Colon, X. G. Zhu, Meeting the global food demand of the future by engineering crop photosynthesis and yield potential. *Cell* **161**, 56–66 (2015).
11. S. Uehara, F. Adachi, Y. Ito-Inaba, T. Inaba, Specific and efficient targeting of cyanobacterial bicarbonate transporters to the inner envelope membrane of chloroplasts in Arabidopsis. *Front. Plant Sci.* **7**, 16 (2016).
12. B. D. Rae et al., Progress and challenges of engineering a biophysical CO_2-concentrating mechanism into higher plants. *J. Exp. Bot.* **68**, 3717–3737 (2017).
13. Y. Fang et al., Engineering and modulating functional cyanobacterial CO_2-fixing organelles. *Front. Plant Sci.* **9**, 739 (2018).
14. B. M. Long et al., Carboxysome encapsulation of the CO_2-fixing enzyme Rubisco in tobacco chloroplasts. *Nat. Commun.* **9**, 3570 (2018).
15. H. L. Wang, B. L. Postier, R. L. Burnap, Alterations in global patterns of gene expression in *Synechocystis* sp. PCC 6803 in response to inorganic carbon limitation and the inactivation of ndhR, a LysR family regulator. *J. Biol. Chem.* **279**, 5739–5751 (2004).
16. Y. L. Jiang et al., Coordinating carbon and nitrogen metabolic signaling through the cyanobacterial global repressor NdhR. *Proc. Natl. Acad. Sci. U.S.A.* **115**, 403–408 (2018).
17. K. A. Selim, F. Haase, M. D. Hartmann, M. Hagemann, K. Forchhammer, P_{II}-like signaling protein SbtB links cAMP sensing with cyanobacterial inorganic carbon response. *Proc. Natl. Acad. Sci. U.S.A.* **115**, E4861–E4869 (2018).
18. J. J. Pengelly et al., Transplastomic integration of a cyanobacterial bicarbonate transporter into tobacco chloroplasts. *J. Exp. Bot.* **65**, 3071–3080 (2014).

Fang et al.
Molecular mechanism underlying transport and allosteric inhibition of bicarbonate transporter SbtA

PNAS | 7 of 8
https://doi.org/10.1073/pnas.2101632118

19. C. C. Wang et al., Structural mechanism of the active bicarbonate transporter from cyanobacteria. Nat. Plants 5, 1184–1193 (2019).
20. C. Poschenrieder et al., Transport and use of bicarbonate in plants: Current knowledge and challenges ahead. Int. J. Mol. Sci. 19, E1352 (2018).
21. K. Forchhammer, K. A. Selim, Carbon/nitrogen homeostasis control in cyanobacteria. FEMS Microbiol. Rev. 44, 33–53 (2020).
22. N. Sui, F. Huang, L. N. Liu, Photosynthesis in phytoplankton: Insights from the newly discovered biological inorganic carbon pumps. Mol. Plant 13, 949–951 (2020).
23. C. Merlin, M. Masters, S. McAteer, A. Coulson, Why is carbonic anhydrase essential to Escherichia coli? J. Bacteriol. 185, 6415–6424 (2003).
24. J. Du, B. Förster, L. Rourke, S. M. Howitt, G. D. Price, Characterisation of cyanobacterial bicarbonate transporters in E. coli shows that SbtA homologs are functional in this heterologous expression system. PLoS One 9, e115905 (2014).
25. S. Khademi et al., Mechanism of ammonia transport by amt/MEP/Rh: Structure of AmtB at 1.35 A. Science 305, 1587–1594 (2004).
26. L. Zheng, D. Kostrewa, S. Bernèche, F. K. Winkler, X. D. Li, The mechanism of ammonia transport based on the crystal structure of AmtB of Escherichia coli. Proc. Natl. Acad. Sci. U.S.A. 101, 17090–17095 (2004).
27. N. Reyes, C. Ginter, O. Boudker, Transport mechanism of a bacterial homologue of glutamate transporters. Nature 462, 880–885 (2009).
28. J. C. Canul-Tec et al., Structure and allosteric inhibition of excitatory amino acid transporter 1. Nature 544, 446–451 (2017).
29. Y. Zhou et al., Cryo-EM structure of the human concentrative nucleoside transporter CNT3. PLoS Biol. 18, e3000790 (2020).
30. G. D. Price, M. C. Shelden, S. M. Howitt, Membrane topology of the cyanobacterial bicarbonate transporter, SbtA, and identification of potential regulatory loops. Mol. Membr. Biol. 28, 265–275 (2011).
31. R. Mancusso, G. G. Gregorio, Q. Liu, D. N. Wang, Structure and mechanism of a bacterial sodium-dependent dicarboxylate transporter. Nature 491, 622–626 (2012).
32. J. A. Kaczmarski et al., Structural basis for the allosteric regulation of the SbtA bicarbonate transporter by the PII-like protein, SbtB, from Cyanobium sp. PCC7001. Biochemistry 58, 5030–5039 (2019).
33. L. Holm, DALI and the persistence of protein shape. Protein Sci. 29, 128–140 (2020).
34. N. J. Hu, S. Iwata, A. D. Cameron, D. Drew, Crystal structure of a bacterial homologue of the bile acid sodium symporter ASBT. Nature 478, 408–411 (2011).
35. C. Lee et al., A two-domain elevator mechanism for sodium/proton antiport. Nature 501, 573–577 (2013).
36. C. Lee et al., Crystal structure of the sodium-proton antiporter NhaA dimer and new mechanistic insights. J. Gen. Physiol. 144, 529–544 (2014).
37. D. Wöhlert, W. Kühlbrandt, O. Yildiz, Structure and substrate ion binding in the sodium/proton antiporter PaNhaP. eLife 3, e03579 (2014).
38. X. Zhou et al., Structural basis of the alternating-access mechanism in a bile acid transporter. Nature 505, 569–573 (2014).
39. M. J. Conroy et al., The crystal structure of the Escherichia coli AmtB-GlnK complex reveals how GlnK regulates the ammonia channel. Proc. Natl. Acad. Sci. U.S.A. 104, 1213–1218 (2007).
40. J. H. Hennacy, M. C. Jonikas, Prospects for engineering biophysical CO2 concentrating mechanisms into land plants to enhance yields. Annu. Rev. Plant Biol. 71, 461–485 (2020).
41. J. Lei, J. Frank, Automated acquisition of cryo-electron micrographs for single particle reconstruction on an FEI Tecnai electron microscope. J. Struct. Biol. 150, 69–80 (2005).
42. S. Q. Zheng et al., MotionCor2: Anisotropic correction of beam-induced motion for improved cryo-electron microscopy. Nat. Methods 14, 331–332 (2017).
43. K. Zhang, Gctf: Real-time CTF determination and correction. J. Struct. Biol. 193, 1–12 (2016).
44. J. Zivanov et al., New tools for automated high-resolution cryo-EM structure determination in RELION-3. eLife 7, e42166 (2018).
45. J. Yang et al., Improved protein structure prediction using predicted interresidue orientations. Proc. Natl. Acad. Sci. U.S.A. 117, 1496–1503 (2020).
46. P. Emsley, K. Cowtan, Coot: Model-building tools for molecular graphics. Acta Crystallogr. D Biol. Crystallogr. 60, 2126–2132 (2004).
47. P. V. Afonine et al., Real-space refinement in PHENIX for cryo-EM and crystallography. Acta Crystallogr. D Struct. Biol. 74, 531–544 (2018).
48. I. W. Davis et al., MolProbity: All-atom contacts and structure validation for proteins and nucleic acids. Nucleic Acids Res. 35, W375–W383 (2007).
49. E. F. Pettersen et al., UCSF ChimeraX: Structure visualization for researchers, educators, and developers. Protein Sci. 30, 70–82 (2021).
50. W. Minor, M. Cymborowski, Z. Otwinowski, M. Chruszcz, HKL-3000: The integration of data reduction and structure solution–From diffraction images to an initial model in minutes. Acta Crystallogr. D Biol. Crystallogr. 62, 859–866 (2006).

8 of 8 | PNAS
https://doi.org/10.1073/pnas.2101632118

Fang et al.
Molecular mechanism underlying transport and allosteric inhibition of bicarbonate transporter SbtA